CARBON ELECTRODE OF HIGH ACTIVITY FOR SO_2 ELECTRO-OXIDATION

RAHUL RAGHUWANSHI

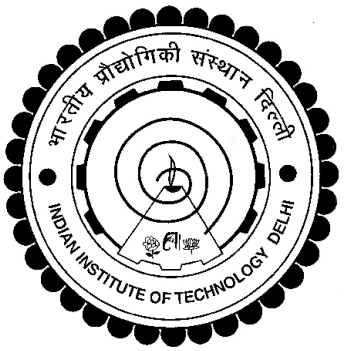

DEPARTMENT OF CHEMICAL ENGINEERING
INDIAN INSTITUTE OF TECHNOLOGY DELHI
NEW DELHI-110016, INDIA

DECEMBER, 2024

Carbon Electrode of High Activity for SO_2 Electro-oxidation

by

Rahul Raghuwanshi

Department of Chemical Engineering

Submitted

in fulfillment of the requirements of degree of Doctor of Philosophy

to the

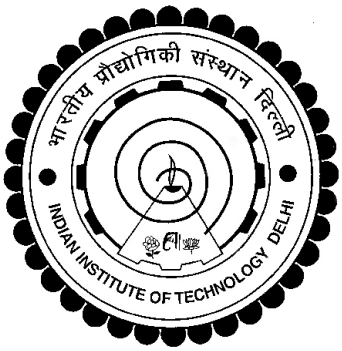

Indian Institute of Technology Delhi

December, 2024

- I dedicate this thesis to my beloved daughter, Kaustubhi. Her presence during these crucial years has been a constant source of joy and inspiration. May this dedication serve as a reminder that the most profound approach to self-learning and discovery lies in the childlike curiosity within the depths of a mature mind -

Certificate

This is to certify that the thesis entitled "**Carbon Electrode of High Activity for SO_2 Electro-oxidation** " submitted by **Rahul Raghuwanshi** to the Indian Institute of Technology Delhi, for the award of the degree of **Doctor of Philosophy** in Chemical Engineering, is a record of bonafide research work carried out by him. Rahul Raghuwanshi has worked under my guidance and supervision and has fulfilled the requirements for the submission of the thesis.

The results contained in this thesis have not been submitted in part or in full to any other university or institute for the award of any degree or diploma.

Anupam Shukla
Department of Chemical Engineering
Indian Institute of Technology, Delhi
India - 110016.

Acknowledgments

I wish to express my deepest gratitude to Dr. Anupam Shukla for his unwavering support and faith in me. His patience, continuous guidance, encouragement, and careful corrections have been invaluable throughout my PhD research journey.

I deeply appreciate the support and encouragement provided by Prof. Ratan Mohan, Prof. Sreedevi Upadhyayula, Prof. Anil Kumar Verma and Prof. Pravin P. Ingole. I would also like to thank Dr. D. Parvatalu, Dr. Saroj Chaudhary, Dr. Ashwini Nirukhe and OECT for their financial support.

I humbly extend my gratitude to my seniors, Mr. Rupesh Tamgadge, Mr. Satirth Sarma, Mrs. Pooja Jangir, and my lab mates, Ms. Isha Atrey, Mrs. Mythili Perapathi, and Mr. Jayant Nagar, for their consistent and wholehearted assistance during these significant years.

Lastly, I offer my thanks to the Almighty God for bestowing upon me the gift of good health. I am profoundly indebted to my beloved parents, Shri Arjun Singh Raghuwanshi and Smt. Asha Raghuwanshi, my wife, Shalini Raghuwanshi, and our precious daughter, Kaustubhi Raghuwanshi, for their unwavering emotional support, boundless love, and countless sacrifices to bring me up to this stage.

Rahul Raghuwanshi

Abstract

Hydrogen, with its high energy density and minimal environmental impact, stands as a promising substitute for fossil fuels in various energy applications. Presently, hydrogen production primarily relies on fossil fuel-based methods, such as steam methane reforming, oil, and coal gasification, which contribute to CO_2, SO_2, and other harmful emissions. Alternatively, water electrolysis, powered by renewable sources like solar, wind, or nuclear energy, offers a greener pathway for hydrogen production. However, water electrolysis faces challenges due to the energy-intensive and sluggish oxygen evolution reaction (OER) at the anode. One efficient alternative is replacing OER with the electrochemical oxidation of sulfur dioxide (SO_2) and water into sulfuric acid (H_2SO_4). This approach finds relevance in processes like the sulfur-iodine (S−I) and hybrid sulfur (HyS) cycles for indirect water-splitting to produce hydrogen. However, the SO_2 electro-oxidation is also not a fast reaction and requires higher potentials for appreciable reaction rate, causing the use of excess energy in electric form.

A fast and efficient SO_2 electro-oxidation requires use of noble metal electrocatalysts namely Pt, Au and Pd. However, noble metals are prone to catalyst poisoning and their utility is limited by large cost, especially for very large scale production. Therefore, it is very attractive to develop a low cost electrode material

with high activity for SO_2 electro-oxidation, which could also be used in other industrially important applications like flue gas desulfurization and SO_2 sensing.

Carbon is a widely used electrode material of low cost, wide availability, good chemical as well as electrochemical stability, and is also available in different forms like graphite, carbon black, pyrographite, activated carbon, glassy carbon, etc. Though carbon is commonly used as support or current collector for electrodes having noble metal-electrocatalyst as active material, it is one of the least active materials for SO_2 electro-oxidation, precluding its use as a standalone electrode for the reaction. In the present study, one of the focuses was on simple electrochemical synthesis of high activity, self-standing carbon fiber paper (CFP) and highly oriented pyrolytic graphite (HOPG) electrodes for SO_2 oxidation. The other focus was to reduce the peak potential, onset potential and charge transfer resistance of the CFP electrodes by optimizing their surface oxygen content via anodization in sulfuric acid and annealing in a nitrogen atmosphere and to optimize the activity of the CFP electrodes to the level of the platinum electrodes.

In the first experimental study, our objective was to improve the activity of a commercially available HOPG sheet by a simple, two-step, electrochemical process. The first step involved the partial exfoliation of HOPG sheet in H_2SO_4 solution for the generation of oxygen functional groups at the electrode surface. This process not only induced structural defects but also resulted in the creation of vertically oriented graphene flakes on the surface, significantly increasing the surface area of the electrode. The second step of the electrode synthesis involved electrochemical reduction of aqueous SO_2 over the partially exfoliated HOPG surface. It resulted in the formation of a sulfur layer over the electrode surface, thereby increasing the activity of the electrode towards SO_2 electro-oxidation. Different process pa-

rameters, such as concentration of the electrolyte (in the first step) and reduction potential (in the second step), were optimized, and the best electrode showed an oxidation peak at a significantly lower potential ($\sim$1.0 V) than the pristine HOPG (>1.2 V).

In the second work, our primary focus was the synthesis of a carbon-based electrode of high activity for SO_2 electro-oxidation. Significant improvements in the activity of the electrode were obtained by introducing surface oxygen functionalities through the anodization of carbon fiber paper in sulfuric acid solution. The mechanical strength of the CFP allows it to be a self-standing electrode of high conductivity. We show that anodization of CFP in sulfuric acid leads to changes on the surface that make it highly active for SO_2 electro-oxidation. Electrodes of varying surface oxygen content (2.90 atomic% to 25.60 atomic%) and relative proportion of different types of oxygen functional groups were obtained by changing the anodization potential and the concentration of sulfuric acid. The activity of the optimal electrode was quantified by exchange current density and charge transfer resistance, respectively. The exchange current density was about 52-times the pristine CFP electrode (2.39 μA cm^{-2} compared to 0.046 μA cm^{-2}). The morphological and structural changes in the electrode on anodization were determined using field emission scanning electron microscopy (FESEM), X-ray diffraction (XRD) and Raman analysis. The chemical analysis of the electrode surface, done using X-ray photoelectron spectroscopy (XPS), showed a strong correlation between the electrode's activity and the ratio of the percentage of hydroxyl groups to the sum of percentages of epoxy and carbonyl groups. The electrode performed well in an accelerated stability test based on cyclic voltammetry for over 1000 cycles.

In the last study, we report a significant increase in the activity of a carbon electrode for SO_2 electro-oxidation by treating its surface to obtain partially reduced graphite oxide (RGO). The RGO surface was formed on a self-standing CFP by a two-step process wherein the CFP was first anodized in sulfuric acid to generate surface oxygen functionalities. The anodized CFP was then annealed in the nitrogen atmosphere to obtain the RGO surface. The structural and chemical features of the electrode surface were varied by an independent variation of anodization potential and annealing temperature. The XPS analysis showed that annealing not only reduced the surface oxygen content of the electrode from $\sim$21 – 26 atomic% to $\sim$3 – 5 atomic% but also allowed tailoring of the oxygen functionalities by preferentially increasing the percentage of hydroxyl groups. The cyclic voltammetry (CV) and electrochemical impedance spectroscopy (EIS) were used to quantify the activity of the electrode for SO_2 electro-oxidation. The electrode's charge transfer resistance for SO_2 electro-oxidation, determined from impedance spectroscopy, showed a linear correlation with the ratio of the percentage of surface hydroxyl groups to the sum of the percentages of epoxy and carbonyl groups. The effect of the activation process on structural characteristics like crystal domain size and defect density was studied using XRD and Raman spectroscopy. For SO_2 electro-oxidation, the activated carbon electrode showed superior performance than the Pt electrode both in terms of substantially lower onset potential (0.26 V versus Ag/AgCl reference electrode compared to 0.35 V for Pt) and 36-times higher exchange current density (6.16 μA cm^{-2} compared to 0.17 μA cm^{-2} for Pt).

Keywords: SO_2 electro-oxidation, CFP, oxygen functionalization, partially reduced graphite oxide, anodization, HOPG, electrochemical surface modifications.

Abstract in Hindi

हाइड्रोजन, अपनी उच्च ऊर्जा घनत्व और न्यूनतम पर्यावरणीय प्रभाव के साथ, विभिन्न ऊर्जा अनुप्रयोगों में जीवाश्म ईंधनों के लिए एक आशाजनक विकल्प के रूप में खड़ा है। वर्तमान में, हाइड्रोजन उत्पादन मुख्य रूप से जीवाश्म ईंधन आधारित विधियों जैसे स्टीम मीथेन रिफॉर्मिंग, तेल और कोयला गैसीकरण पर निर्भर है, जो CO_2, SO_2 और अन्य हानिकारक उत्सर्जन में योगदान करते हैं। इसके विपरीत, जल इलेक्ट्रोलिसिस, जो सौर, पवन या परमाणु ऊर्जा जैसे नवीकरणीय स्रोतों द्वारा संचालित होती है, हाइड्रोजन उत्पादन के लिए एक हरित मार्ग प्रदान करती है। हालांकि, जल इलेक्ट्रोलिसिस में एनोड पर ऊर्जा-गहन और धीमी ऑक्सीजन विकास प्रतिक्रिया (OER) के कारण चुनौतियाँ हैं। इसका एक प्रभावी विकल्प OER को सल्फर डाइऑक्साइड (SO_2) और पानी के विद्युत रासायनिक ऑक्सीकरण द्वारा सल्फ्यूरिक एसिड (H_2SO_4) में बदलना है। यह दृष्टिकोण हाइड्रोजन उत्पादन के लिए अप्रत्यक्ष जल-विभाजन के लिए सल्फर-आयोडीन (S–I) और हाइब्रिड सल्फर (HyS) चक्र जैसी प्रक्रियाओं में प्रासंगिक है। हालांकि, SO_2 इलेक्ट्रो-ऑक्सीडेशन भी एक तेज़ प्रतिक्रिया नहीं है और उचित प्रतिक्रिया दर के लिए उच्च वोल्टेज की आवश्यकता होती है, जिससे विद्युत ऊर्जा का अधिक उपयोग होता है।

SO_2 इलेक्ट्रो-ऑक्सीडेशन को तेज़ और कुशल बनाने के लिए नोबल मेटल इलेक्ट्रोकैटेलिस्ट जैसे Pt, Au और Pd का उपयोग किया जाता है। हालांकि, नोबल मेटल्स कैटालिस्ट पॉइज़निंग के प्रति संवेदनशील होते हैं और इनकी उपयोगिता बड़ी लागत के –

कारण सीमित होती है, विशेष रूप से बड़े पैमाने पर उत्पादन के लिए। इसलिए, SO_2 इलेक्ट्रो-ऑक्सीडेशन के लिए उच्च सक्रियता वाले कम लागत के इलेक्ट्रोड सामग्री को विकसित करना बहुत आकर्षक है, जिसका उपयोग फ्ल्यू गैस डीसल्फराइजेशन और SO_2 सेंसिंग जैसे अन्य औद्योगिक रूप से महत्वपूर्ण अनुप्रयोगों में भी किया जा सकता है।

कार्बन एक व्यापक रूप से उपयोग की जाने वाली इलेक्ट्रोड सामग्री है, जो कम लागत, व्यापक उपलब्धता, अच्छी रासायनिक और विद्युत-रासायनिक स्थिरता प्रदान करती है। यह विभिन्न रूपों में उपलब्ध है, जैसे ग्रेफाइट, कार्बन ब्लैक, पायरोग्राफाइट, एक्टिवेटेड कार्बन, ग्लासी कार्बन, आदि। हालांकि, कार्बन आमतौर पर इलेक्ट्रोड में समर्थन या करंट कलेक्टर के रूप में उपयोग होता है, जिसमें नोबल मेटल-इलेक्ट्रोकैटेलिस्ट सक्रिय सामग्री के रूप में कार्य करता है। यह SO_2 इलेक्ट्रो-ऑक्सीडेशन के लिए सबसे कम सक्रिय सामग्री में से एक है, जिससे इसे इस प्रतिक्रिया के लिए एक स्वतंत्र इलेक्ट्रोड के रूप में उपयोग करना मुश्किल हो जाता है।

इस अध्ययन में, ध्यान सरल विद्युत-रासायनिक संश्लेषण के माध्यम से उच्च सक्रियता वाले, सेल्फ-स्टैंडिंग कार्बन फाइबर पेपर (CFP) और उच्च अभिविन्यास वाले पायरोलिटिक ग्रेफाइट (HOPG) इलेक्ट्रोड विकसित करने पर केंद्रित था। दूसरा उद्देश्य CFP इलेक्ट्रोड की सतह ऑक्सीजन कॉन्टेंट को सल्फ्यूरिक एसिड में एनोडाइजेशन और नाइट्रोजन वातावरण में एनीलिंग द्वारा अनुकूलित करके उनकी गतिविधि को प्लेटिनम इलेक्ट्रोड के स्तर तक बढ़ाना था।

पहले प्रयोगात्मक अध्ययन में, हमारा उद्देश्य एक सरल, दो-चरणीय, विद्युत रासायनिक प्रक्रिया द्वारा वाणिज्यिक रूप से उपलब्ध HOPG शीट की गतिविधि में सुधार करना था। पहले चरण में, H_2SO_4 घोल में HOPG शीट का आंशिक एक्सफोलिएशन शामिल था, जो इलेक्ट्रोड सतह पर ऑक्सीजन फ़ंक्शनल समूहों की पीढ़ी के लिए किया गया था। इस प्रक्रिया ने न केवल संरचनात्मक दोष उत्पन्न किए, बल्कि सतह पर लंबवत उन्मुख ग्रेफीन फ्लेक्स का निर्माण भी किया, जिससे इलेक्ट्रोड का सतही क्षेत्रफल काफी बढ़ गया। इलेक्ट्रोड संश्लेषण का दूसरा चरण आंशिक रूप से एक्सफोलिएटेड HOPG सतह पर जलीय SO_2 के विद्युत रासायनिक कमीकरण

से संबंधित था। इसने इलेक्ट्रोड सतह पर सल्फर परत के निर्माण का परिणाम दिया, जिससे SO_2 इलेक्ट्रो-ऑक्सीडेशन के प्रति इलेक्ट्रोड की गतिविधि बढ़ गई। विभिन्न प्रक्रिया मापदंडों, जैसे इलेक्ट्रोलाइट की सांद्रता (पहले चरण में) और कम वोल्टेज (दूसरे चरण में), को अनुकूलित किया गया। सबसे अच्छे इलेक्ट्रोड ने ऑक्सीकरण शिखर को प्रारंभिक HOPG (>1.2 V) की तुलना में काफी कम वोल्टेज (~1.0 V) पर दिखाया।

दूसरे अध्ययन में, हमारा मुख्य ध्यान SO_2 इलेक्ट्रो-ऑक्सीडेशन के लिए उच्च सक्रियता वाले कार्बन-आधारित इलेक्ट्रोड के संश्लेषण पर था। सल्फ्यूरिक एसिड घोल में कार्बन फाइबर पेपर के एनोडाइजेशन के माध्यम से सतह ऑक्सीजन फ़ंक्शनल समूहों को पेश करके इलेक्ट्रोड की गतिविधि में महत्वपूर्ण सुधार प्राप्त किए गए। CFP की यांत्रिक ताकत इसे उच्च चालकता वाले एक सेल्फ-स्टैंडिंग इलेक्ट्रोड के रूप में उपयोग करने की अनुमति देती है। हमने दिखाया कि सल्फ्यूरिक एसिड में CFP का एनोडाइजेशन सतह पर ऐसे बदलाव करता है जो इसे SO_2 इलेक्ट्रो-ऑक्सीडेशन के लिए अत्यधिक सक्रिय बनाते हैं।

कुंजी शब्द: SO_2 इलेक्ट्रो-ऑक्सीडेशन, CFP, ऑक्सीजन कार्यात्मकता, आंशिक रूप से घटित ग्रेफाइट ऑक्साइड, एनोडाइज़ेशन, HOPG, विद्युत-रासायनिक सतह संशोधन।

Contents

Certificate i

Acknowledgement iii

Abstract v

1 Introduction 1
- 1.1 Background . . . 1
- 1.2 Research objectives . . . 8
- 1.3 Thesis organization . . . 9

2 Literature review 11
- 2.1 Reaction mechanism . . . 13
- 2.2 Carbon electrodes for SO_2 electro-oxidation . . . 18
- 2.3 Performance of modified carbon electrodes . . . 21
- 2.4 Summary . . . 23

3 Surface modified HOPG electrode 27
- 3.1 Introduction . . . 28
- 3.2 Experimental methods . . . 31
  - 3.2.1 Electrode preparation . . . 31
  - 3.2.2 Material Characterizations . . . 32
  - 3.2.3 Electrochemical Analysis . . . 33
- 3.3 Results and discussions . . . 35
  - 3.3.1 Electrochemical treatment of HOPG . . . 35
  - 3.3.2 Material characterizations . . . 37
  - 3.3.3 Electrochemical measurements . . . 45
- 3.4 Conclusion . . . 50

4 Anodized CFP electrode **53**
4.1 Introduction . . . 54
4.2 Experimental methods . . . 57
4.2.1 Electrode preparation . . . 57
4.2.2 Electrochemical Analysis . . . 57
4.2.3 Material Characterizations . . . 61
4.3 Results and discussions . . . 61
4.3.1 Effect of anodization on CFP surface . . . 61
4.3.2 Faradaic activity of the anodized CFP electrodes . . . 65
4.3.3 Physical and chemical characterizations of the CFP electrodes 72
4.4 Conclusion . . . 85

5 Partially reduced graphite oxide **87**
5.1 Introduction . . . 88
5.2 Experimental methods . . . 91
5.2.1 Synthesis of RGO-CFP electrodes . . . 91
5.2.2 Material Characterizations . . . 93
5.2.3 Electrochemical Analysis . . . 93
5.3 Results and discussions . . . 98
5.3.1 Physical and chemical characterizations . . . 98
5.3.2 Electrochemical characterizations . . . 109
5.3.3 SO_2 electro-oxidation in a full cell . . . 118
5.3.4 Conclusion . . . 120

6 Conclusions **123**

A Appendix A **127**
A.0.1 Electrochemical characterizations . . . 127
A.0.2 Four-probe analysis . . . 133
A.0.3 Structural and chemical characterizations . . . 134
A.0.4 Reaction mechanism . . . 139
A.0.5 Stability analysis . . . 141

B Appendix B **145**
B.0.1 Structural and chemical characterizations . . . 145
B.0.2 Four-probe analysis . . . 155
B.0.3 Electrochemical characterizations . . . 158
B.0.4 Stability analysis . . . 165

References **171**

Publications from the Thesis **187**

Author's Biography **189**

List of Figures

1.1 Primary energy consumption by fuels in 2021, (a) Global consumption and (b) Indian consumption. A break-up of the (c) global hydrogen demand and (d) global hydrogen production in 2021. 3
1.2 A schematic diagram of hydrogen-water cycle. 4
1.3 A schematic diagram of S–I cycle. 6

2.1 Appleby and Pichon [27] reported current density for different electrode materials (Rotating disc electrodes) at 0.7 V versus SHE in 44wt% H_2SO_4 with dissolved SO_2 (1 atm.) at 50°C. 20

3.1 CV curves (12^{th} cycle) at 50 mV/s scan rates: (a) in supporting electrolyte (0.1 M H_2SO_4) between 0.6–0.7 V (versus Ag/AgCl), and (b) in 0.5 M HCl electrolyte between −0.25–0.15 V (versus Ag/AgCl). The inset figure in plot (b) shows the hydrogen adsorption region. 35
3.2 A schematic of the experimental set-up and the electrochemical modification process for the activation of HOPG electrode. 36
3.3 Electrode synthesis step-2: (a) chronoamperograms and (b) cyclic voltammograms (3rd cycle) in 0.05 M Na_2SO_3 solution in 0.1 M H_2SO_4 at the negative polarization potential limits of −0.1 V, −0.3 V and −0.5 V (versus Ag/AgCl). Partially activated (PART. ACT.) HOPG electrode is modified in 0.1 M H_2SO_4 solution at the negative polarization potential limits of −0.5 V. 38
3.4 FESEM images: Top view of (a) pristine HOPG and (b) HOPG partially exfoliated in 1 M H_2SO_4. Side view of (c) pristine HOPG and (d) partially exfoliated HOPG. Top view of electrode after (e) first synthesis step and (f) second synthesis step. The inset of part b shows the top view of HOPG partially exfoliated in 0.1 M H_2SO_4 and that of parts e and f shows the magnified view of the corresponding images. 39

3.5 (a) XRD diffraction peaks corresponding to 002, 004 and 006 plane and (b) Raman spectrum corresponding to D band, G band and 2D band of pristine, partially exfoliated (PART. EXF.) and activated (ACT3) HOPG electrodes. 41
3.6 (a) XPS survey spectra, (b) high resolution S_{2P} peak along with the deconvoluted component and (c) high resolution C_{1S} peak of pristine, partially exfoliated and activated HOPG electrodes along with the deconvoluted component. 44
3.7 Cyclic voltammograms (5^{th} cycle, 10 mV/s) in the electroactive electrolyte and supporting electrolyte for (a) Pristine HOPG, (b) HOPG partially exfoliated in 1.0 M H2SO4 and (c) electrode (ACT3) activated at $-0.5\,V$ (vs Ag/AgCl) in 0.05 M Na_2SO_3 solution in 0.1 M H_2SO_4 after its partial exfoliation in 1.0 M H_2SO_4. (d) compare the CV curves of pristine and surface modified HOPG electrodes. 48
3.8 Cyclic voltammograms (5^{th} cycle, 10 mV/s) in the electroactive electrolyte for surface modified HOPG electrodes prepared by (a) identical partial exfoliation (first) step, but sulfur deposition carried out at different (negative) potentials in the second synthesis step and (b) partial exfoliation carried out in H_2SO_4 solutions of different pH or concentration in the first synthesis step, but identical sulfur deposition (second) step. (d) compare the CV curves of Pt and ACT3 electrodes. 49

4.1 A schematic diagram of three electrode set-up 59
4.2 CV curves (4^{th} cycle, 10 mV/s scan rate) for (a) pristine CFP electrodes cycled in the background electrolyte (BACK. E.) between $0\,V - 1.2\,V$ (P.CFP1.2V) and $0\,V - 1.5\,V$ (P.CFP1.5V). The inset figure is the magnified view of the voltammogram for P.CFP1.2V electrode that clearly shows the reversible redox peaks. The CV curves recorded at similar conditions in the electroactive electrolyte (EL. ACT. E.) are shown for (b) P.CFP1.5V and (c) P.CFP1.2V electrodes, and the inset figures show the magnified view of the selected region of CV curves recorded in the background and electroactive electrolyte, respectively. 63

4.3 Cyclic voltammograms at 10 mV/s scan rate in the electroactive electrolyte of (a) CFP electrodes anodized in 6M H_2SO_4 for different times, and (b) CFP electrodes anodized for 2400 s in H_2SO_4 solutions of different concentrations. Impedance spectra of CFP electrodes acquired in the electroactive electrolyte at 0.8 V DC bias, in the frequency range 1 MHz to 0.1 Hz as (c) Nyquist plots, and (d) Bode plots; (e) equivalent circuit used to model the impedance data. The model simulated impedance is shown as solid curves of part (c) and (d). 68
4.4 (a) IR corrected LSV curves for pristine and anodized CFP electrodes at a rotation rate of 36 RPM; (b) Tafel curves obtained by plotting the logarithm of kinetic current (J_K) for SO_2 electro-oxidation versus overpotential (η) in the electroactive electrolyte. 71
4.5 FESEM images of (a) P.CFP, (b) OPT.CFP, (c) 12.0MCFP, and (d) CFP2.0V electrodes. The inset of the figures shows the magnified images of a carbon fiber. 74
4.6 (a) XRD patterns, and (b) magnified view of 002 diffraction peaks for P.CFP, 0.1MCFP, OPT.CFP, 12.0MCFP, and CFP2.0V electrodes. . . . 75
4.7 (a) Raman spectra along with the magnified view of the D and G bands showing the deconvolution of the G band region into G and D′ bands for the CFP electrodes; (b) the variation of the D to G band intensity ratio (I_D/I_G), and D to D′ band intensity ratio ($I_D/I_{D'}$) for the CFP electrodes; (c) a plot of I_D/I_G versus $I_{D'}/I_G$ for the CFP electrodes. . . 76
4.8 (a) XPS survey spectra, and (b) the C_{1S} peak along with its deconvolution to component peaks for P.CFP, 0.1MCFP, OPT.CFP, 12.0MCFP and CFP2.0V electrodes. The deconvoluted components peaks provided quantitative measure of the different oxygen functional groups on the surface and (c) a plot of charge transfer resistance (R_{CT}) versus the ratio of the percentage of hydroxyl groups to the sum of the percentages of epoxy and carbonyl groups. 78

4.9 Accelerated stability test of the OPT.CFP electrode performed by (a) cycling in the potential window 0.6 – 1.3 V at 50 mV/s scan rate in an electrolyte solution of 0.05 M Na_2SO_3 and 0.1 M H_2SO_4; (b) impedance spectra of OPT.CFP electrode (as Nyquist plot) at DC bias of 0.8 V, and in the frequency range 1 MHz to 0.1 Hz recorded after 10^{th}, 260^{th}, 510^{th}, 760^{th} and 1010^{th} CV cycles. The solid curves in the Nyquist plot are the impedance simulated using the equivalent circuit of Figure 4.3e. (c) Chronoamperometry at 0.7, 0.9 and 1.1 V (versus Ag/AgCl), in three consecutive runs of 3000 s each. 83

5.1 A schematic illustration of the CFP treatment process. 92
5.2 FESEM images of (a) PC, (b) PC700, (c) 3.0VC, and (d) 3.0VC700 electrodes. The inset of the figures shows the magnified image of a carbon fiber. 100
5.3 XRD patterns of (a) pristine CFP (PC), anodized CFP (A-CFP), and (b) RGO-CFP electrodes. Magnified view of (c) 002 diffraction peaks and (d) 004 diffraction peaks for PC, A-CFP, and RGO-CFP electrodes. 101
5.4 Raman spectra along with the magnified view of the D and G bands showing the deconvolution of the G band region into G and D′ bands for the (a) PC, A-CFP, and (b) RGO-CFP electrodes. (c) The variation of the D to G band intensity ratio (I_D/I_G), and (d) the plot of I_D/I_G versus $I_{D'}/I_G$ intensity ratio is shown for the CFP electrodes. 103
5.5 XPS survey spectra for the (a) PC, A-CFP and (b) RGO-CFP electrodes. The C_{1S} peak along with its deconvolution to component peaks for the (c) PC, A-CFP and (d) RGO-CFP electrodes. 105
5.6 Cyclic voltammograms (4^{th} Cycle) at 10 mV/s scan rate in the electroactive electrolyte for (a) RGO-CFP electrodes anodized at potentials $\leq$ 1.5 V and (b) RGO-CFP electrodes anodized at potentials $\geq$ 2.0 V. Impedance spectra of RGO-CFP electrodes shown in parts (a) and (b) are presented as Nyquist curves (acquired in the electroactive electrolyte at 0.3 V DC bias and frequency 1 MHz to 0.01 Hz) in parts (c) and (d). The equivalent circuit of part (e) was used to model the impedance data and (f) is a plot of charge transfer resistance (R_{CT}) versus the ratio of the percentage of hydroxyl groups to the sum of the percentages of epoxy and carbonyl groups. 111

5.7 Tafel plot for Pt and RGO-CFP electrodes obtained by plotting (a) the logarithm of kinetic current (J_K) for SO_2 electro-oxidation versus overpotential (η) and (b) shows the plot of calculated TOF for the reaction versus overpotential in the electroactive electrolyte. 115

5.8 Accelerated stability test of the 3.0VC900 electrode performed by (a) cycling in the potential window 0.2 V−0.7 V at 50 mV/s scan rate in an electrolyte solution of 0.05 M Na_2SO_3 and 0.1 M H_2SO_4; (b) impedance spectra of 3.0VC900 electrode (as Nyquist plot) at DC bias of 0.3 V, and in frequency range 1 MHz to 0.01 Hz recorded after 10^{th}, 260^{th}, 510^{th}, 760^{th} and 1010^{th} CV cycles. The solid curves in the Nyquist plot are the impedance simulated using the equivalent circuit of Figure 5.6e. (c) Chronoamperometry at 0.4 V (versus Ag/AgCl), in four consecutive runs of 3000 s each for 3.0VC900 electrode. 117

5.9 The image of an H-type cell used during the electrolysis experiments. . . 119

A.1 (a) Cyclic voltammograms (4^{th} Cycle, 10 mV/s scan rate) in the electroactive electrolyte for CFP electrodes anodized in 6 M H_2SO_4 at different potentials. Impedance spectra in the form of Nyquist curves for (b) CFP1.0V and OPT.CFP electrodes (in the electroactive electrolyte) and (c) CFP2.0V electrodes (in the electroactive and supporting electrolyte), as well as (d) Bode impedance and phase angle curves of the electrodes in the electroactive electrolyte were acquired at a DC bias of 0.8 V and between 1 MHz to 0.1 Hz frequency. Equivalent circuit of Figure 4.3e was used to model the impedance data of CFP1.0V and OPT.CFP electrodes and Equivalent circuits (I) and (II) of part (c) were used to model the impedance data of CFP2.0V electrode. The inset figure in part (d) demonstrate the bode impedance and phase angle curves of CFP2.0V electrode. 128

A.2 Nyquist curves of OPT.CFP electrode obtained in (a) background electrolyte and (b) electroactive electrolyte, at DC bias of 0.8 V, and between 1 MHz to 0.1 Hz frequency. The inset figures demonstrate the equivalent circuit models and Nyquist curves in the high-frequency region (1.0 MHz to 35.0 Hz). The equivalent circuit model simulated impedance is shown as the solid curves. 129

A.3 LSV curves of (a) P.CFP, (b) 3.0MCFP, (c) OPT.CFP and (d) 9.0MCFP recorded in the electroactive electrolyte at 10 mV/s scan rate and 16−49 RPM. 131

A.4 Inverse of current density ($1/j$) versus inverse of square root of rotation rate ($1/\omega^{0.5}$) from LSV data shown in Figure A.3 for CFP electrodes at (a) 0.975 V, (b) 1.00 V, (c) 1.025 V, (d) 1.05 V and (e) 1.075 V versus Ag/AgCl reference electrode. The kinetic current is recorded from the intersection of $1/j$ versus $1/\omega^{0.5}$. 132
A.5 Four-point probe analysis of pristine and anodized CFP electrodes. The slope of voltage versus current curve represents the ohmic resistance of the CFP electrodes. 133
A.6 EDX Elemental mapping of (a) P.CFP, (b) 0.1MCFP, (c) OPT.CFP, (d) 12.0MCFP and (e) CFP2.0V electrodes surface. 134
A.7 EDX Elemental analysis of (a) Surface Blister, and (b) Bare Surface of OPT.CFP electrode. 135
A.8 XRD spectra of (a) 004, and (b) 006 diffraction peaks, as obtained for the P.CFP, 0.1MCFP, OPT.CFP, 12.0MCFP and CFP2.0V electrodes. . 136
A.9 Fitted and deconvoluted XPS spectra of high resolution C_{1S} peaks for (a) P.CFP, (b) 0.1MCFP, (c) OPT.CFP, (d) 12.0MCFP and (e) CFP2.0V electrodes. 137
A.10 Fitted and deconvoluted XPS spectra of high resolution O_{1S} peak of P.CFP, 0.1MCFP, OPT.CFP, 12.0MCFP and CFP2.0V electrodes. . . . 138
A.11 Fitted and deconvoluted XPS spectra of high resolution (a) S_{2P} and (b) N_{1S} peaks of P.CFP, 0.1MCFP, OPT.CFP, 12.0MCFP and CFP2.0V electrodes. 139
A.12 Proposed reaction scheme for SO_2 oxidation over RGO-CFP electrode surface involving an active role of the surface hydroxyl groups. 140
A.13 (a) XPS survey spectra and (b) deconvoluted C1S peak of the CYCLED OPT.CFP electrode after accelerated stability test. 142

B.1 FESEM images for the side view of (a) PC and (b) 3.0VC electrode. . . 146
B.2 EDX Elemental mapping of (a) PC, (b) PC700, (c) 3.0VC and (d) 3.0VC700 electrodes surface. 147
B.3 Magnified view of 006 diffraction peak for (a) A-CFP and (b) RGO-CFP electrodes. (c) ratio of 004 and 002 diffraction peak area, and (d) FWHM of 002 diffraction peaks of the CFP electrodes. The 002 and 004 diffraction peaks are shown in Figure 5.3 of the main text. 148
B.4 XRD patterns of (a) 3.0VC, 3.0VC500, 3.0VC700 and 3.0VC900. Magnified view of (b) 004 diffraction peaks and (c) 006 diffraction peaks for the above mentioned electrodes. 149

B.5 Raman spectra along with the magnified view of the D and G bands showing the deconvolution of the G band region into G and D′ bands for (a) 2.0VC, 3.5VC, 2.0VC900 and 3.5VC900 electrodes. (b) Plot of the D to G band intensity ratio (I_D/I_G) for the A-CFP and RGO-CFP electrodes shown in part (a). 150
B.6 Raman spectra along with the magnified view of the D and G bands showing the deconvolution of the G band region into G and D′ bands for (a) A-CFP and RGO-CFP electrodes anodized at 3.0 V and annealed at different temperatures. (b) Plot of the D to G band intensity ratio (I_D/I_G) for the A-CFP and RGO-CFP electrodes shown in part (a). . . 151
B.7 (a) XPS survey spectra, and high resolution C_{1S} component peaks along with its deconvolution to component peaks for (b) 3.0VC1000, (c) 3.5VC900 and (d) 2.0VC900 electrodes. 152
B.8 Deconvoluted XPS spectra of high resolution C_{1S} component peaks for (a) PC, (b) 1.0VC, (c) 2.0VC and (e) 3.0VC electrodes. 153
B.9 Deconvoluted XPS spectra of high resolution C_{1S} component peaks for (a) PC700, (b) 1.0VC700, (c) 2.0VC700, (d) 3.0VC700, (e) 3.0VC900 and (e) 3.0VC500 electrodes. 154
B.10 Deconvoluted XPS spectra of high resolution S_{2P} peak for (a) PC, PC700, A-CFP, and (b) RGO-CFP electrodes. 155
B.11 Deconvoluted XPS spectra of high resolution N_{1S} peak for (a) PC, PC700, A-CFP, and (b) RGO-CFP electrodes. 156
B.12 Four-point probe analysis of (a) pristine CFP, A-CFP and (b) RGO-CFP electrodes. 157
B.13 (a) Cyclic voltammograms (4^{th} cycle, 10 mV/s scan rate) in the supporting or background electrolyte (BACK. E.) and electroactive electrolyte (EL. ACT. EL.) for 3.0VC900 electrode. (b) The Nyquist curve of 3.0VC900 electrode recorded in the supporting electrolyte at 0.3 V DC bias and between 1 MHz to 0.01 Hz frequency is modeled with the equivalent circuit shown at the top right corner of the plot. The inset figure at the bottom right corner of part (b) shows the Nyquist curve of the electrode in the electroactive electrolyte modeled with the equivalent circuit model of Figure 5.6e of Chapter 5. The model simulated impedance is shown as the solid curves. 160

B.14 (a) Cyclic voltammograms (4^{th} cycle, 10 mV/s scan rate) in the electroactive electrolyte for Pt, 3.0VC900 and 3.0VC1000 electrodes. The Nyquist curve in the electroactive electrolyte for (b) Pt electrode at 0.3 V DC bias and between 1 MHz to 0.1 Hz frequency is modeled with the equivalent circuit shown at the top right corner of the plot. The equivalent circuit model simulated impedance is shown as the solid curves. (c) Cyclic voltammograms (4^{th} cycle, 10 mV/s scan rate) in the electroactive electrolyte for 1.0VC, 1.5VC and 2.0VC electrodes. 162
B.15 LSV curves of (a) 3.0VC1000, (b) 3.5VC900, (c) 3.0VC900, (d) 2.0VC900 and (e) Pt recorded in the electroactive electrolyte at 5 mV/s scan rate and 300 – 600 RPM. (f) LSV curves recorded at 500 RPM are shown for all the electrodes. 163
B.16 Inverse of current density ($1/j$) versus inverse of square root of rotation rate ($1/\omega^{0.5}$) from LSV data shown in Figure B.15 for RGO-CFP and Pt electrodes at (a) 0.38, (b) 0.40, (c) 0.42 and (d) 0.45 V versus Ag/AgCl reference electrode. The kinetic current is recorded from the intersection of $1/j$ versus $1/\omega^{0.5}$. 164
B.17 Cyclic voltammogram of (a) Pt electrode and (b) RGO-CFP electrodes in 0.1 M H_2SO_4 at 5 mV/s scan rate. The curve shown in the inset of part (a) corresponds to the hydrogen adsorption region. 166
B.18 ECSA normalized integrated charge (Q) obtained from chronoamperometry at various potentials are plotted at first 50 s, 100 s, 150 s, 200 s, 250 s and 300 s versus the square root of time for (a) 3.0VC1000, (b) 3.5VC900, (c) 3.0VC900, (d) 2.0VC900 and (e) Pt electrode. (f) The intercept of Q versus $\text{Time}^{1/2}$ is plotted at their corresponding potentials for the RGO-CFP and Pt electrodes. 167
B.19 (a) XPS survey spectra and (b) deconvoluted C_{1S} peak of the CYCLED 3.0VC900 electrode after accelerated stability test. 169

List of Tables

2.1 A comparison of the activity of various electrodes in terms of peak potential and onset potentials obtained for SO_2 electro-oxidation. 25

3.1 Experimental conditions used for the activation of the HOPG electrode. 32
3.2 A comparative analysis of FWHM and diffraction peak area ratios (A_{004}/A_{002} and A_{006}/A_{002}) from the XRD analysis of pristine, partially exfoliated and activated HOPG electrodes. 40
3.3 A comparative analysis of I_D/I_G and I_{2D}/I_G peak intensity ratios and G peak position from the Raman spectra of pristine, partially exfoliated and activated HOPG electrodes. 42
3.4 The elemental compositions and O/C ratio of pristine, partially exfoliated and activated HOPG electrodes. 45
3.5 The surface compositions of C−S−C and C−SO_X−C functional groups, as obtained for pristine, partially exfoliated and activated HOPG electrodes from the area of deconvoluted S_{2P} peaks shown in Figure 3.6b. . . 45
3.6 The surface compositions of C=C, C–C, C–OH, C–O–C, and C=O functional groups, as obtained for pristine, partially exfoliated and activated HOPG electrodes from the area of deconvoluted component shown in Figure 3.6c. 45
3.7 Electrochemical surface area of HOPG electrodes. 46

4.1 Anodization conditions used for the synthesis of CFP electrodes. 58
4.2 Electrochemical surface area of CFP electrodes. 60
4.3 The best-fit parameters of the equivalent circuit model of Figure 4.3e used to model the impedance response of pristine and anodized CFP electrodes. The model parameter values included in the table are R_S, R_ϕ, R_{CT}, Q_ϕ, α_ϕ and Z_W. 70

4.4 The exchange current density (j_o) for the pristine and anodized CFP electrodes. 71
4.5 Ohmic resistance of the electrodes measured using four-point probe method 72
4.6 XPS elemental compositions and O/C ratio of pristine and anodized CFP electrodes. 79
4.7 The surface compositions of C=C, C−C, C−OH, C−O−C, and C=O functional groups, as obtained for (a) P.CFP, (b) 0.1MCFP, (c) OPT.CFP, (d) 12.0MCFP and (e) CFP2.0V electrodes from area of deconvoluted C_{1S} component peaks shown in Figure 4.8b. 80

5.1 Experimental conditions used for the synthesis of RGO-CFP electrodes. 92
5.2 ECSA of pristine and RGO-CFP electrodes. 95
5.3 The elemental compositions and O/C ratio of pristine (PC), anodized (A-CFP) and RGO-CFP electrodes determined from XPS. 106
5.4 The surface compositions of C=C, C−C, C−OH, C−O−C, and C=O functional groups for PC, A-CFP and RGO-CFP electrodes, as obtained from the area of deconvoluted C_{1S} component peaks shown in Figures 5.5c−5.5d. 108
5.5 Sheet resistance of the PC, A-CFP and RGO-CFP electrodes measured using the four-point probe method. 108
5.6 The best-fit parameters of the equivalent circuit model of Figure 5.6e used to simulate the impedance response of Pt, pristine (PC), anodized (A-CFP), and RGO-CFP electrodes. 112
5.7 Exchange current density (j_o) of the Pt and the CFP electrodes activated at different conditions. 115
5.8 The anolyte concentration data, current efficiency (η_I) and charge (Q) supplied during the electrolysis in the anodic compartment of H-Cell at 0.4 V versus Ag/AgCl. 120

A.1 The best-fit parameters (R_S, R_ϕ, R_{CT}, Q_ϕ, α_ϕ and Z_W) of the equivalent circuit model of Figures 4.3e and A.1c used to model the impedance response of CFP1.0V, and CFP2.0V electrodes. 130
A.2 The best-fit parameters (Q_{DL}, α_{DL} and χ^2) of the equivalent circuit model of Figure 4.3e and A.1c used to model the impedance response of pristine and anodized CFP electrodes. 130
A.3 The surface compositions of C=O and C–O functional groups, as obtained for P.CFP, 0.1MCFP, OPT.CFP, 12.0MCFP and CFP2.0V electrodes from the area of deconvoluted O_{1S} peaks shown in Figure A.10. . 138

A.4 The surface compositions of Carbon-Sulfur (C–S) and Carbon-Nitrogen (C–N) based functional groups, as obtained for P.CFP, 0.1MCFP, OPT.CFP, 12.0MCFP and CFP2.0V electrodes from the area of deconvoluted S_{2P} and N_{1S} peaks shown in Figure A.11. 140

A.5 The best-fit parameters (R_S, R_ϕ, R_{CT}, Q_ϕ, α_ϕ and Z_W) of the equivalent circuit model of Figure 4.3e used to model the impedance response of OPT.CFP electrode after 10^{th}, 260^{th}, 510^{th}, 760^{th} and 1010^{th} CV cycles (for accelerated stability test) in 0.05 M Na_2SO_3 solution in 0.1 M H_2SO_4 electrolyte. 141

A.6 The best-fit parameters (Q_{DL}, α_{DL} and χ^2) of the equivalent circuit model of Figure 4.3e used to model the impedance response of OPT.CFP electrode after 10^{th}, 260^{th}, 510^{th}, 760^{th} and 1010^{th} CV cycles (for accelerated stability test). 142

A.7 The surface compositions of elements i.e., C, O, N and S, as obtained for the CYCLED OPT.CFP electrode after accelerated stability test. . . 143

A.8 The surface compositions of C=C, C−C, C−OH, C−O−C, and C=O functional groups, as obtained for the CYCLED OPT.CFP electrode after accelerated stability test, from the area of deconvoluted C_{1S} peaks shown in Figure A.13b. 143

B.1 XPS elemental compositions and O/C ratios for 3.0VC1000, 3.5VC900 and 2.0VC900 electrodes. 152

B.2 The surface compositions of C=C, C−C, C−OH, C−O−C, and C=O functional groups for PC, A-CFP and RGO-CFP electrodes, as obtained from the area of deconvoluted C_{1S} component peaks shown in Figures B.7. 153

B.3 The surface compositions of carbon-sulfur (C–S) and carbon-nitrogen (C–N) based functional groups, as obtained for PC, A-CFP and RGO-CFP electrodes, from the area of deconvoluted S_{2P} and N_{1S} peaks shown in Figures B.10 and B.11. 156

B.4 Peak potential and onset potential (at 200 μA cm^{-2}) for CFP electrodes and Pt from the CV curves shown in Figure B.14a and Figures 5.6a–b of Chapter 5. 159

B.5 The best fit parameters (Q_{DL}, α_{DL} and χ^2) obtained from the equivalent circuit model (as shown in Figure 5.6e of Chapter 5) simulated impedance response of CFP electrodes and Pt. 161

B.6 The integrated charge (Q_T) obtained from the CV curves of Figures B.17a–b, charge due to electric double layer capacitance (Q_{EDLC}) obtained from the slope of curves shown in Figure B.18f, and the number of active sites (n') calculated by using Equation B.1. 166

B.7 The best-fit parameters (R_S, R_ϕ, R_{CT}, Q_ϕ, α_ϕ and Z_W) of the equivalent circuit model of Figure 5.6e used to model the impedance response of 3.0VC900 electrode after 10^{th}, 260^{th}, 510^{th}, 760^{th} and 1010^{th} CV cycles (for accelerated stability test) in 0.05 M Na_2SO_3 solution in 0.1 M H_2SO_4 electrolyte. 168

B.8 The best-fit parameters (Q_{DL}, α_{DL} and χ^2) of the equivalent circuit model of Figure 5.6e used to model the impedance response of 3.0VC900 electrode after 10^{th}, 260^{th}, 510^{th}, 760^{th} and 1010^{th} CV cycles (for accelerated stability test). 168

B.9 The surface compositions of elements i.e., C, O, N and S, as obtained for the CYCLED 3.0VC900 electrode after accelerated stability test. . . 169

B.10 The surface compositions of C=C, C–C, C–OH, C–O–C, and C=O functional groups, as obtained for the CYCLED 3.0VC900 electrode after accelerated stability test, from the area of deconvoluted C_{1S} component peaks shown in Figure B.19b. 169

Nomenclature and list of abbreviations

Symbol	Definition
E	Applied potential (V)
E^o	Equilibrium (or thermodynamic reversible) potential (V)
a	Activity (Bq)
z	Number of electrons transferred
r, s, u and v	Stoichiometric coefficients
R	Universal gas constant (J mol^{-1} K^{-1})
F	Farday constant (C mol^{-1})
T	Temperature (°C or K)
P	Pressure (bar or atm.)
K_I	First dissociation constant
K_{II}	Second dissociation constant
v/v	Volume/volume
λ	Wavelength (nm)
θ	Angle of diffraction (°)
C	Capacitance (F)
C_H	Helmholtz capacitance (F cm^{-2})
f	Applied frequency (Hz)
Z''	imaginary part of impedance (Ω or Ω cm^2)
Z'	imaginary part of impedance (Ω or Ω cm^2)
A	Area of electrode (cm^2)
A_{CV}	Area enclosed by CV curve (C)

A_{Pt}	Real surface area of platinum electrode (cm^2)
ν	Scan rate (V/s)
ΔV	Voltage window (V)
V	Voltage (V)
e	Electron or elementary charge (C)
d_m	Surface metal atom density of platinum (cm^{-2})
Q	Electric charge (C)
Q_m	Charge associated with monolayer (hydrogen) adsorption (C)
I	Current (A)
I_D, I_G, I_{2D}, $I_{D'}$	Intensity of Raman bands
R_{CT}	Charge transfer resistance (Ω cm^2)
R_S	Solution resistance (Ω cm^2)
R_ϕ	Resistance due to CPE_ϕ (Ω cm^2)
Z_W	Warburg impedance ($s^{0.5}\,\Omega^{-1}\,cm^{-2}$)
Q_{DL}	Magnitude of impedance for CPE_{DL} ($s^{\alpha}\Omega^{-1}\,cm^{-2}$)
Q_ϕ	Magnitude of impedance for CPE_ϕ ($s^{\alpha}\Omega^{-1}\,cm^{-2}$)
ω	angular frequency (rad/s)
α	Factor associated with the phase of the impedance
χ^2	Goodness of fit
ϕ_{max}	Maximum magnitude of phase angle (°)
j	Current density (A cm^{-2})
j_o	Exchange current density (A cm^{-2})
R_{SH}	Sheet resistance (Ω $sq.^{-1}$)
TOF	Turnover frequency (s^{-1})
J_K	Kinetic current density (A cm^{-2})
n'	Number of active sites (mol cm^{-2})
Q_{EDLC}	Charge due to electric double layer capacitance (C cm^{-2})
Q_T	Integrated charge obtained from CV curves (C cm^{-2})
M_T	Theoretical increase in the amount of acid (mols)
M_E	Actual increase in the amount of acid (mols)
C_I	Initial concentration of anolyte (H_2SO_4 solution) (M)
C_F	Final concentration of anolyte (H_2SO_4 solution) (M)
V'	Volume of anolyte (H_2SO_4 solution) (ml)
η_I	faradaic efficiency (%)

Abbreviation	Description
HOPG	Highly oriented pyrolytic graphite
ACT	Activated HOPG
PART. EXF. HOPG	Partially exfoliated HOPG
PART. ACT. HOPG	Partially activated HOPG
S-HOPG	Sulfur covered pristine HOPG
CFP	Carbon fiber paper
P.CFP or PC	Pristine CFP
OPT.CFP	Optimally anodized CFP
GO	Graphene oxide
RGO	Partially reduced graphite oxide
A-CFP	Anodized CFP
RGO-CFP	RGO surface formed on self standing CFP by annealing
OER	Oxygen evolution reaction
S−I cycle	Sulfur-iodine cycle
HyS cycle	Hybrid sulfur cycle
Pt	Platinum
Au	Gold
Pd	Palladium
Rh	Rhodium
Ir	Iridium
Cr	Chromium
Cu	Copper
Al	Aluminium
M	Metal
Pt−M	Pt based bimetallic catalyst
M−O	Metal oxide
M−OH	Metal hydroxide
Pt/C	Platinum supported on carbon
Pd/C	Palladium supported on carbon
TiO_2	Titanium dioxide
Pt/Ti	Platinized titanium
Au/TiO_2	Gold nanoparticles supported on titania
GC	Glassy carbon
IG	Impregnated graphite

NG	Natural graphite
GR	Graphite rod
BRX	Activated carbon
ExCO	Carbon prepared from cracked carbon monoxide
EGO	Electrochemical graphite oxide
FESEM	Field emission scanning electron microscopy
EDX	Energy dispersive X-ray
XRD	X-ray diffraction
XPS	X-ray photoelectron spectroscopy
CV	Cyclic voltammetry or cyclic voltammogram
EIS	Electrochemical impedance spectroscopy
LSV	Linear sweep voltammetry
RHE	Reversible hydrogen electrode
SHE	Standard hydrogen electrode
BET	Brunauer-Emmett-Teller
eps	Electrons per site
ECSA	Electrochemical surface area
FWHM	Full width at half maximum
3D	Three-dimensional
RDE	Rotating disk electrode
DC	Direct current
AC	Alternating current
BACK. E.	Background or supporting electrolyte
EL. ACT. E.	Electroactive electrolyte
CPE	Constant phase element
$\mathrm{CPE_{DL}}$	CPE for the double layer capacitance
CPE_{ϕ}	CPE for the pseudocapacitance
Z_{CPE}	Impedance of constant phase element
DoS	Electronic density of state